Received XX Month, XXXX; revised XX Month, XXXX; accepted XX Month, XXXX; Date of publication XX Month, XXXX; date of current version XX Month, XXXX.

Digital Object Identifier 10.1109/OJCOMS.2026.xxxxx

Channel Estimation and Relay Selection for Space-Air-Ground-Sea Integrated Networks

Waruni Bandara[1], *Student Member, IEEE,* Omar Maraqa[1], Ahmed A. Al-Habob[1], *Senior Member, IEEE,* Quang Nhat Le[1], *Member, IEEE,* Octavia A. Dobre[1], *Fellow, IEEE*, and Trung Q. Duong[1], *Fellow, IEEE*

[1]Faculty of Engineering and Applied Science, Memorial University, St. John's, NL A1B 3X5, Canada, (e-mail: {balagallehit, omaraqa, aaaalhabob, qnle, odobre, tduong}@mun.ca)

CORRESPONDING AUTHOR: TRUNG Q. DUONG (tduong@mun.ca)

This work was supported in part by the Canada Excellence Research Chair (CERC) Program CERC-2022-00109, in part by the Natural Sciences and Engineering Research Council of Canada (NSERC) Discovery Grant Program RGPIN-2025-04941, in part by the Canada Research Chairs (CRC) Program CRC-2022-00187, Canada First Research Excellence Fund (CFREF) Transforming Climate Action, Grant TCA-LRP-20241-MUN-1.3-03, and in part by CFREF Clean Arctic Shipping Initiative, Grant CFREF-2022-00062.

ABSTRACT Reliable communication over oceans and in remote areas remains challenging because most wireless networks depend on land-based infrastructure. Space–air–ground–sea integrated networks (SAGSINs) provide a promising solution by integrating space, aerial, terrestrial, and maritime network components to extend coverage beyond the reach of land-based networks. In this paper, we consider a maritime relay-assisted SAGSIN where a sea-surface station (SS) communicates with a base station (BS) through one relay selected from three candidate platforms: an onshore station, a high-altitude platform, and a satellite (SAT). Since these relay links operate in different propagation environments and network segments, accurate channel estimation and relay selection become challenging. The proposed framework considers least squares (LS), linear minimum mean square error (LMMSE), and an adapted denoising convolutional neural network (DnCNN)-based estimator for channel estimation over heterogeneous maritime relay links. The DnCNN-based estimator learns the nonlinear mapping between the initial channel estimate and the corresponding refined channel estimate, thereby reducing estimation errors caused by noise and limited pilot observations. The refined channel estimates are then used to support relay selection, so that the SS can choose a suitable relay for forwarding its data to the BS. The simulation results confirm that the adapted DnCNN-based estimator generally provides lower normalized mean square error than the traditional LS and LMMSE estimators, especially at low transmit power and short pilot length. The results further show that the proposed relay selection method achieves an end-to-end data rate close to the perfect channel state information benchmark. These results confirm that accurate channel estimation improves relay selection and enhances maritime communication performance.

INDEX TERMS Space–air–ground–sea integrated networks, maritime communication, channel estimation, relay selection, deep learning.

I. Introduction

Future sixth generation (6G) wireless networks are expected to provide reliable communication everywhere by connecting terrestrial and non-terrestrial networks [1]. However, terrestrial infrastructure alone cannot guarantee seamless communication in remote and infrastructure-limited environments, such as oceans, islands, and disaster-affected regions. To overcome these coverage limitations, 6G systems are expected to integrate space, air, ground, and sea segments into a unified communication framework, known as a space-air-ground-sea integrated network (SAGSIN) [1], [2]. This integrated network is particularly important for maritime communication, where sea-surface station (SS) may operate far from the coastline and direct communication with the core network can become weak or unavailable [1], [3]. In such environments, relay-assisted SAGSIN can support the connection between the SS and the core network, thereby improving maritime coverage and reliability. Beyond conventional relay-assisted architectures, reconfigurable intelligent surfaces (RISs) and stacked intelligent metasurfaces (SIMs) have recently gained significant attention for future wireless networks. By using multiple programmable metasurface layers, SIMs can support wave-domain signal processing, near-field beam training, and wideband transceiver design [4]–[6].

In maritime relay-assisted SAGSIN, different relay platforms can provide different coverage advantages. For example, onshore stations (OSs) can support near-shore communication, aerial platforms such as high altitude platforms (HAPs) can provide wide-area coverage, and satellites (SATs) can support long-distance offshore communication. Selecting the most suitable relay requires accurate knowledge of the channel conditions, since inaccurate channel estimates can lead to incorrect relay selection and degrade the overall system performance. However, channel estimation is challenging in this environment because heterogeneous relay links can experience different propagation conditions. Near-shore links may be affected by sea-surface reflection and two-ray propagation [3], whereas aerial and satellite links may suffer from stronger path loss, platform mobility, Doppler effects, and atmospheric attenuation [7], [8]. Therefore, reliable channel state information (CSI) estimation is important for evaluating link quality and supporting effective relay selection in maritime communication.

Traditional channel estimation methods, such as least square (LS) and linear minimum mean square error (LMMSE), are widely used because of their simple implementation [9]–[11]. However, their performance can degrade when the received pilot signals are noisy or when the channel has complex propagation behavior. Learning-based estimators, such as deep residual learning models, can improve estimation accuracy by learning the residual error between noisy estimates and true channels [12]. Although several studies have addressed channel modeling, channel estimation, and relay selection in integrated networks, existing works have investigated these problems separately [10], [13]–[15]. Specifically, several channel estimation works focus on a single network segment, such as air–ground or satellite–ground communication [10], [11], while several relay-selection studies assume that full CSI is available at the relay-selection stage [14], [15]. However, this assumption is difficult to satisfy in maritime relay-assisted SAGSINs because the relay decision should be made using estimated channel conditions. Therefore, the impact of channel estimation errors on relay selection performance in maritime relay-assisted SAGSINs remains insufficiently studied.

To address this gap, this paper proposes a joint channel estimation and relay selection framework for maritime relay-assisted SAGSIN. In the proposed framework, traditional estimators and a learning-based estimator are first used to estimate the channels between the SS and the candidate relays. The estimated channel information is then used to evaluate the quality of each relay link and select the most suitable relay for data transmission. The main contributions of this paper are summarized as follows:

1) We investigated a maritime relay-assisted SAGSIN, where an SS communicates with the core network through heterogeneous OS, HAP, and SAT relays.
2) We evaluate the traditional LS and LMMSE estimators together with a residual denoising convolutional neural network (DnCNN)-based estimator for the heterogeneous SS–OS, SS–HAP, and SS–SAT links.
3) We design two relay-selection methods for the considered maritime relay-assisted SAGSIN. The first method selects the relay based on the estimated SS–relay data rate, whereas the second method selects the relay based on the estimated end-to-end data rate.
4) We provide detailed simulation results to evaluate the impact of channel estimation accuracy on relay selection and end-to-end data-rate performance. The results compare the LS, LMMSE, and DnCNN-based estimators in terms of normalized mean square error (NMSE) and achievable data rate under different simulation settings, including the SS transmit power, pilot length, and relay-link conditions. In addition, the relay selection probability is investigated to show how the preferred relay changes with the SS location in the considered maritime service area.

The rest of this paper is organized as follows. Section II reviews the existing related works that cover channel modeling, channel estimation, and relay selection in integrated networks. Section III presents the considered maritime relay-assisted SAGSIN system model and the corresponding channel models for the heterogeneous relay links. Section IV introduces the channel estimation and relay selection framework, including the LS, LMMSE, and DnCNN-based estimators and the two relay-selection methods. Section V provides the simulation results. Finally, Section VI concludes the paper.

II. Related Work

Reliable maritime communication through SAGSIN requires accurate modeling of heterogeneous links, reliable channel estimation, and effective relay selection. Related works have addressed these aspects from different perspectives. To summarize their scope, Table 1 compares

Table 1: Comparison of existing related works

References	Space Segment	Air Segment	Maritime Segment	Channel Modeling	Channel Estimation	Relay Selection
[1]	✓	✓	✓	✓	–	–
[3]	✓	✓	✓	✓	–	–
[7]	✓	✓	–	✓	–	–
[10]	✓	✓	–	✓	✓	–
[11]	–	✓	–	✓	✓	–
[12]	–	–	–	–	✓	–
[13]	✓	✓	–	✓	–	–
[14]	✓	–	–	✓	–	✓
[15]	✓	–	–	✓	–	✓
[16]	–	✓	–	✓	✓	–
[17]	–	✓	–	✓	–	✓
[18]	✓	–	–	✓	–	–
[19]	✓	–	–	✓	–	–
[20]	✓	✓	✓	✓	–	✓
[21]	✓	✓	–	✓	–	✓
[22]	✓	–	✓	✓	–	–
[23]	✓	✓	–	✓	–	✓
[24]	✓	–	–	✓	✓	–
Proposed work	✓	✓	✓	✓	✓	✓

the related works in terms of the considered network segments, including the space, air, and maritime segments, as well as channel modeling, channel estimation, and relay selection.

Several works have investigated channel modeling in SAGSIN. Early works modeled space-air-ground integrated network (SAGIN) by considering space, aerial, and ground links with different propagation conditions and platform mobility for outage performance analysis [13]. Later, SAGSIN channel models were extended to maritime scenarios by using different models for different links, such as international telecommunication union (ITU)-based models for shore-to-sea segments, Rician fading for HAP-to-sea segments, and Shadowed-Rician fading for satellite-to-sea segments [1]. End-to-end LEO-satellite-aided shore-to-ship communication was also investigated by modeling the maritime and satellite links using Rician and Shadowed-Rician fading, respectively [22]. More recent studies investigated more accurate satellite and aerial channel modeling by considering practical effects such as atmospheric loss, weather attenuation, earth rotation, mobility, elevation angle, and urban propagation environments [7], [18], [19]. These studies show that channel behavior in SAGSIN is highly heterogeneous and depends strongly on the considered network segment and propagation environment.

Relay selection is important in SAGSIN because maritime users can be served through different relay platforms, such as terrestrial stations, aerial platforms, and satellites. Since these relays operate at different network segments and experience different channel conditions, they may provide different communication quality. Therefore, selecting the most suitable relay is necessary to improve the reliability and performance of maritime communication. To address this problem, existing studies have used different relay-selection criteria. For instance, relay selection in SAGSIN has been performed by choosing the relay with the strongest received power among heterogeneous relay candidates [1]. For maritime terminals in [20], aerial relay selection has also been studied by selecting the relay that provides the highest end-to-end channel capacity. More recently, relay selection has been considered for cooperative air–ground communication systems [17]. In SAGIN, maximum-signal-to-noise-interference ratio (SINR)-based relay-node selection has also been studied [21]. Joint unmanned aerial vehicle (UAV) trajectory planning and LEO-satellite selection was investigated in [23], where the satellite was selected according to the achievable data rate and its remaining visibility time. These works show that relay and satellite selection in integrated networks has mainly been addressed using received power, capacity, SINR, achievable rate, visibility time, and cooperative relaying criteria. However, the effect of channel estimation on relay selection in maritime SAGSIN has received limited attention.

Channel estimation is also essential for reliable communication because the receiver depends on accurate CSI to evaluate the channel condition. In the literature, channel behavior and channel estimation have been studied for individual segment links. For example, air–ground channels have been characterized through measurement-based studies [16], and channel-estimation-based reliable transmission has also been investigated for air–ground communication [11]. However, when moving toward integrated networks, channel estimation becomes more challenging because the links may belong to different network segments. For example, channel estimation has been studied for UAV–satellite communication in SAGINs, which mainly considers the air and space segments [10]. For LEO satellite massive multiple-input multiple-output (MIMO)-OFDM communication, a two-stage channel-estimation method was developed in [24] by exploiting the angle-delay-domain structure of the satellite channel. These studies show the importance of accurate CSI in dynamic aerial and space-related links. However, most existing channel-estimation studies focus on one or two network segments, rather than maritime relay-assisted SAGSIN. As a result, channel estimation across heterogeneous maritime relay links remains less explored.

The above studies provide important foundations for integrated network modeling, relay selection, and channel estimation. However, these topics are often studied separately. This separation is not sufficient for maritime relay-assisted SAGSINs, where the relay decision depends on the estimated channel information. Therefore, the effect of channel-estimation accuracy on relay selection remains an important open issue. To address this gap, this work considers a maritime relay-assisted SAGSIN framework that jointly integrates channel modeling, channel estimation, and relay selection.

III. System and Channel Models

This section presents the relay-assisted SAGSIN architecture considered for maritime communication and the corresponding channel models, as illustrated in Fig. 1. The SS communicates with the ground base station (BS) through one selected relay. The relay is selected from three candidates, namely an OS, a HAP, and a SAT. The relay set is denoted by $\mathcal{K} = \{\mathrm{OS}, \mathrm{HAP}, \mathrm{SAT}\}$, where $k \in \mathcal{K}$ represents a relay candidate. Each relay candidate and the BS are equipped with a uniform rectangular array (URA), while the SS is equipped with a single antenna. The URA at relay k consists of $N_k = N_{k,x}N_{k,y}$ antenna elements, where $N_{k,x}$ and $N_{k,y}$ denote the numbers of antenna elements along the x- and y-axes, respectively. Similarly, the URA at the BS consists of $N_{\mathrm{BS}} = N_{\mathrm{BS},x}N_{\mathrm{BS},y}$ antenna elements, where $N_{\mathrm{BS},x}$ and $N_{\mathrm{BS},y}$ denote the numbers of antenna elements along the x- and y-axes, respectively.

Let $\mathbf{h}_{\mathrm{SS},k}$ denote the channel from the SS to relay k, and let $\mathbf{H}_{k,\mathrm{BS}}$ denote the channel from relay k to the BS. Since the relays in $\mathcal{K}$ are located in different network segments, the corresponding SS–relay links experience heterogeneous propagation conditions. Accordingly, these links are modeled as shown in (2), which appears at the top of the next page. Specifically, the SS-to-OS link is represented by a two-ray propagation model that accounts for the dominant line-of-sight (LoS) path and the sea-surface-reflected path [3]. The SS–

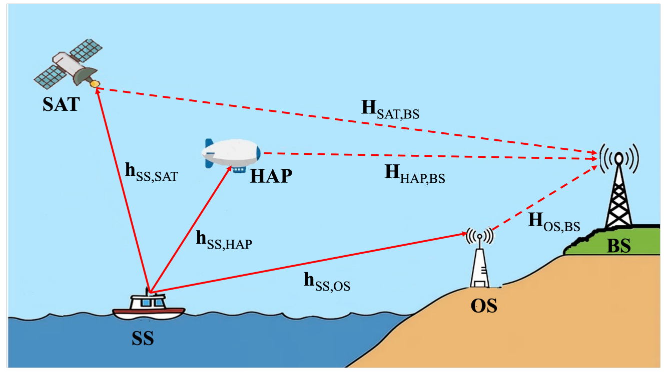

Fig. 1: System model of the considered maritime relay-assisted SAGSIN.

HAP link is modeled using distance-dependent free-space path loss [25], whereas the SS-to-SAT link accounts for both free-space path loss and rain attenuation [3], [26]. In addition, each link incorporates Rician small-scale fading.

Additionally in (2), λ_k denotes the carrier wavelength of the SS-to-relay k link, and $d_{\mathrm{SS},k}$ denotes the Euclidean distance between the SS and relay k. The parameters h_{SS} and h_k denote the heights of the SS and relay k, respectively, while G_{SS} and G_k denote their corresponding antenna gains. For the SS-to-SAT link, r_k denotes the linear rain attenuation factor. Let $\tilde{r}_k = 10\log_{10}(r_k)$ denote the rain attenuation, where $\tilde{r}_k \sim \mathcal{N}(\mu_r, R_r^2)$, and μ_r and R_r denote its mean and standard deviation, respectively. Furthermore, $K_{\mathrm{SS},k}$ denotes the Rician K-factor of the SS–relay k link, while $\mathbf{h}_{\mathrm{SS},k}^{\mathrm{LoS}}$ and $\mathbf{h}_{\mathrm{SS},k}^{\mathrm{NLoS}}$ denote the LoS and non-line-of-sight (NLoS) components, respectively. The LoS component is modeled using the relay-side URA steering vector corresponding to the arrival direction from the SS to relay k, and is expressed as [25]

$$\mathbf{h}_{\mathrm{SS},k}^{\mathrm{LoS}} = \mathbf{a}_k^{\mathrm{x}}\left(\phi_{\mathrm{SS},k}^{\mathrm{x}}\right) \otimes \mathbf{a}_k^{\mathrm{y}}\left(\phi_{\mathrm{SS},k}^{\mathrm{y}}\right), \tag{1}$$

where $\otimes$ denotes the Kronecker product. The relay URA steering vectors along the x- and y-axes are given by [25]

$$\left[\mathbf{a}_k^{\mathrm{x}}\left(\phi_{\mathrm{SS},k}^{\mathrm{x}}\right)\right]_m = \frac{e^{-j\nu_k D_k (m-1)\phi_{\mathrm{SS},k}^{\mathrm{x}}}}{\sqrt{N_{k,x}}}, \quad m = 1, \ldots, N_{k,x}, \tag{3}$$

$$\left[\mathbf{a}_k^{\mathrm{y}}\left(\phi_{\mathrm{SS},k}^{\mathrm{y}}\right)\right]_n = \frac{e^{-j\nu_k D_k (n-1)\phi_{\mathrm{SS},k}^{\mathrm{y}}}}{\sqrt{N_{k,y}}}, \quad n = 1, \ldots, N_{k,y}, \tag{4}$$

where m and n denote the antenna-element indices along the x- and y-axes of the relay URA, respectively. The parameter $\nu_k = 2\pi/\lambda_k$ represents the wavenumber, where $\lambda_k = c/f_k$ is the carrier wavelength, c is the speed of light, and f_k is the carrier frequency of the SS-to-relay k link. In addition, D_k denotes the antenna spacing at relay k. The variables $\phi_{\mathrm{SS},k}^{\mathrm{x}}$ and $\phi_{\mathrm{SS},k}^{\mathrm{y}}$ denote the direction cosines along the x- and y-axes, respectively, and are given by $\phi_{\mathrm{SS},k}^{\mathrm{x}} = \cos(\theta_{\mathrm{SS},k}^{\mathrm{el}})\cos(\theta_{\mathrm{SS},k}^{\mathrm{az}})$ and

$$\mathbf{h}_{\mathrm{SS},k} = \begin{cases} \dfrac{\lambda_k}{2\pi d_{\mathrm{SS},k}} \sin\left(\dfrac{2\pi h_{\mathrm{SS}} h_k}{\lambda_k d_{\mathrm{SS},k}}\right) \sqrt{G_{\mathrm{SS}} G_k} \left(\sqrt{\dfrac{K_{\mathrm{SS},k}}{K_{\mathrm{SS},k}+1}}\, \mathbf{h}_{\mathrm{SS},k}^{\mathrm{LoS}} + \sqrt{\dfrac{1}{K_{\mathrm{SS},k}+1}}\, \mathbf{h}_{\mathrm{SS},k}^{\mathrm{NLoS}}\right), & k = \mathrm{OS}, \\ \dfrac{\lambda_k}{4\pi d_{\mathrm{SS},k}} \sqrt{G_{\mathrm{SS}} G_k} \left(\sqrt{\dfrac{K_{\mathrm{SS},k}}{K_{\mathrm{SS},k}+1}}\, \mathbf{h}_{\mathrm{SS},k}^{\mathrm{LoS}} + \sqrt{\dfrac{1}{K_{\mathrm{SS},k}+1}}\, \mathbf{h}_{\mathrm{SS},k}^{\mathrm{NLoS}}\right), & k = \mathrm{HAP}, \\ \dfrac{\lambda_k}{4\pi d_{\mathrm{SS},k}} \sqrt{\dfrac{G_{\mathrm{SS}} G_k}{r_k}} \left(\sqrt{\dfrac{K_{\mathrm{SS},k}}{K_{\mathrm{SS},k}+1}}\, \mathbf{h}_{\mathrm{SS},k}^{\mathrm{LoS}} + \sqrt{\dfrac{1}{K_{\mathrm{SS},k}+1}}\, \mathbf{h}_{\mathrm{SS},k}^{\mathrm{NLoS}}\right), & k = \mathrm{SAT}. \end{cases} \tag{2}$$

$\phi^{\mathrm{y}}_{\mathrm{SS},k} = \cos(\theta^{\mathrm{el}}_{\mathrm{SS},k})\sin(\theta^{\mathrm{az}}_{\mathrm{SS},k})$, where $\theta^{\mathrm{az}}_{\mathrm{SS},k}$ and $\theta^{\mathrm{el}}_{\mathrm{SS},k}$ denote the azimuth and elevation angles of the SS-to-relay k link, respectively. These angles are obtained from the node geometry as $\theta^{\mathrm{az}}_{\mathrm{SS},k} = \mathrm{atan2}(y_k - y_{\mathrm{SS}}, x_k - x_{\mathrm{SS}})$ and $\theta^{\mathrm{el}}_{\mathrm{SS},k} = \mathrm{atan2}\left(z_k - z_{\mathrm{SS}}, \sqrt{(x_k - x_{\mathrm{SS}})^2 + (y_k - y_{\mathrm{SS}})^2}\right)$, where $(x_{\mathrm{SS}}, y_{\mathrm{SS}}, z_{\mathrm{SS}})$ and (x_k, y_k, z_k) denote the positions of the SS and relay k, respectively. The scattered NLoS component is modeled as a circularly symmetric complex Gaussian random vector, i.e., $\mathbf{h}^{\mathrm{NLoS}}_{\mathrm{SS},k} \sim \mathcal{CN}\left(\mathbf{0}, \frac{1}{N_k}\mathbf{I}_{N_k}\right)$, for $k \in \mathcal{K}$. The considered channels follow a block-fading model, where the channel remains constant during each short transmission block [27]–[29]. Following [3], [30], [31], the dominant Doppler shift is assumed to be estimated and compensated at the receiver before channel estimation. Therefore, the residual Doppler effect is neglected within each transmission block. In addition, platform altitude variations, atmospheric absorption, shadowing, sea-state-dependent reflection changes, and time-varying rain attenuation are not explicitly modeled, consistent with the assumptions adopted in [1], [3], [25], [26].

Based on these channel models, the channel $\mathbf{h}_{\mathrm{SS},k}$ depends on the SS position from the shore and varies across relay candidates. Therefore, this channel needs to be estimated for each relay candidate, and the resulting channel information is used to select the best relay, denoted by $k^\star$. The proposed channel estimation and relay-selection procedure is described in the next section.

IV. Channel Estimation and Relay Selection

The proposed methodology consists of two main stages: channel estimation and relay selection. In the first stage, each relay estimates its corresponding SS–relay k channel. For this purpose, three channel estimation methods are considered, namely LS, LMMSE, and the DnCNN-based estimator. In the second stage, the estimated SS–relay k channels are used to select the best relay. Two relay-selection methods are considered: the first selects the relay based on the estimated SS–relay k data rate, whereas the second selects the relay based on the estimated end-to-end data rate. After the best relay is selected, the selected relay forwards the decoded data from the SS to the BS.

A. Channel Estimation

To estimate the SS–relay k channels, the SS transmits a pilot sequence $\mathbf{P} = [p_1, p_2, \ldots, p_C] \in \mathbb{C}^{1\times C}$ to the relays, where C denotes the pilot length. The pilot sequence satisfies $\mathbf{P}\mathbf{P}^H = CP_p$, where P_p denotes the transmit power per pilot symbol. In the considered simulations, the pilot-symbol power is set equal to the SS transmit power, i.e., $P_p = P_{\mathrm{SS}}$. For relay $k \in \mathcal{K}$, the received pilot signal is modeled as [32], [33]

$$\mathbf{Y}_k = \mathbf{h}_{\mathrm{SS},k}\mathbf{P} + \mathbf{N}_k, \tag{5}$$

where $\mathbf{Y}_k \in \mathbb{C}^{N_k\times C}$ denotes the received pilot signal matrix, and $\mathbf{N}_k \in \mathbb{C}^{N_k\times C}$ denotes the additive white Gaussian noise (AWGN) matrix. Each entry of $\mathbf{N}_k$ is independently distributed as $\mathcal{CN}(0, \sigma_k^2)$, where $\sigma_k^2 = N_0 W_{\mathrm{SS},k}$ is the noise variance at relay k. Here, N_0 denotes the noise power spectral density, and $W_{\mathrm{SS},k}$ denotes the bandwidth of the SS–relay k link. Using the received pilot signal in (5), each relay estimates its corresponding SS–relay k channel. The following subsections describe the three channel estimation methods considered in this work.

1) LS Channel Estimator

The LS channel estimator estimates the channel by minimizing the squared error between the received pilot signal and the reconstructed pilot signal. Based on the received pilot model in (5), the LS estimate of the SS–relay k channel is given by [12]

$$\widehat{\mathbf{h}}^{\mathrm{LS}}_{\mathrm{SS},k} = \mathbf{Y}_k\mathbf{P}^\dagger, \tag{6}$$

where $\mathbf{P}^\dagger = \mathbf{P}^H\left(\mathbf{P}\mathbf{P}^H\right)^{-1}$ denotes the pseudoinverse of the pilot sequence $\mathbf{P}$.

2) LMMSE Channel Estimator

The LMMSE channel estimator is considered because it uses channel statistical information [12] to obtain a more accurate estimate than LS estimation. Unlike the LS estimator, the LMMSE estimator exploits the channel covariance matrix and noise variance to suppress the effect of noise. Based on the received pilot model in (5), the LMMSE estimate of the SS–relay k channel is given by [12]

$$\widehat{\mathbf{h}}^{\mathrm{LMMSE}}_{\mathrm{SS},k} = \mathbf{R}_{\mathrm{SS},k}\left(\mathbf{P}\mathbf{P}^H\mathbf{R}_{\mathrm{SS},k} + \sigma_k^2\mathbf{I}_{N_k}\right)^{-1}\mathbf{Y}_k\mathbf{P}^H, \tag{7}$$

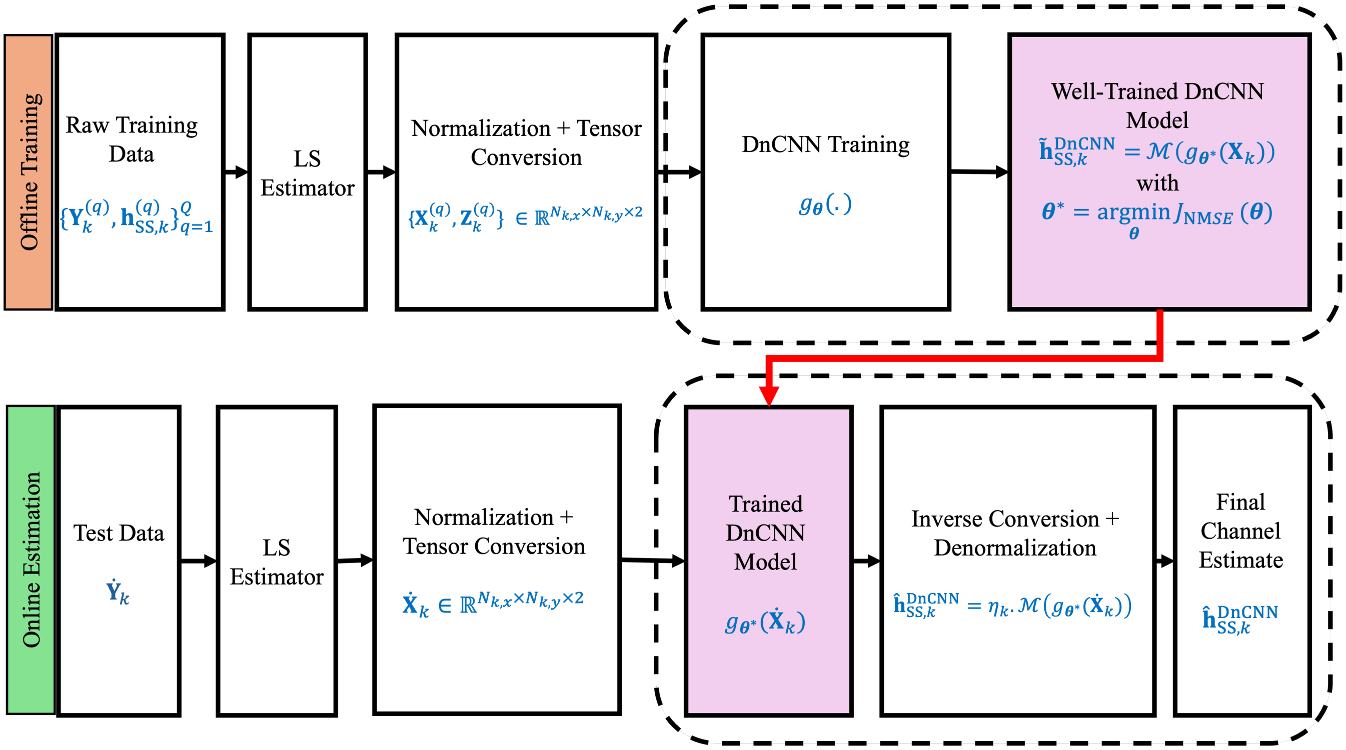

Fig. 2: DnCNN-based channel estimation framework for the heterogeneous links, including offline training and online estimation stages.

where $\mathbf{R}_{\mathrm{SS},k} = \mathbb{E}\left[\mathbf{h}_{\mathrm{SS},k}\mathbf{h}_{\mathrm{SS},k}^{H}\right]$ is the covariance matrix of the SS–relay k channel.

3) DnCNN-Based Channel Estimator

In addition to the traditional LS and LMMSE estimators, this work adopts a DnCNN-based channel estimator for the SS–relay k link, following the denoising-based learning approach in [12]. Compared with [12], the adopted DnCNN estimator differs in its training objective, channel normalization, dataset generation, network configuration, and integration with relay selection. The LS estimate is first used as a coarse channel estimate because it can be obtained directly from the received pilot signal without requiring prior channel statistics. However, under low signal-to-noise ratio (SNR) conditions, the LS estimate can contain significant estimation error. Therefore, the DnCNN estimator treats the LS estimate as a noisy observation of the true channel and refines it using a residual denoising network. Based on the LS estimate in (6), the noisy channel observation at relay k can be written as

$$\widehat{\mathbf{h}}_{\mathrm{SS},k}^{\mathrm{LS}} = \mathbf{h}_{\mathrm{SS},k} + \mathbf{e}_k, \tag{8}$$

where $\mathbf{e}_k \in \mathbb{C}^{N_k \times 1}$ denotes the LS estimation error. Hence, the channel estimation problem can be viewed as a denoising problem, where the objective is to recover $\mathbf{h}_{\mathrm{SS},k}$ from the noisy observation $\widehat{\mathbf{h}}_{\mathrm{SS},k}^{\mathrm{LS}}$. The DnCNN estimator has two stages: offline training and online estimation. Fig. 2 illustrates the overall DnCNN-based channel estimation framework.

a: Offline Training

In the offline stage, simulated pilot observations and true channels are used to construct the training dataset. The LS estimator is first applied to the simulated received pilot observations to generate noisy channel estimates. These noisy LS estimates are then paired with the corresponding true channels to train the DnCNN. For relay k, the resulting training dataset is defined as

$$\mathcal{D}_k = \left\{\left(\widehat{\mathbf{h}}_{\mathrm{SS},k}^{\mathrm{LS},(q)}, \mathbf{h}_{\mathrm{SS},k}^{(q)}\right)\right\}_{q=1}^{Q}, \tag{9}$$

where Q is the number of training samples and q is the training sample index. In each pair, $\widehat{\mathbf{h}}_{\mathrm{SS},k}^{\mathrm{LS},(q)}$ is the noisy LS estimate obtained from $\mathbf{Y}_k^{(q)}$, and $\mathbf{h}_{\mathrm{SS},k}^{(q)}$ is the corresponding true channel. In the online stage, the trained DnCNN model obtained from the offline training stage is directly applied to a new test dataset to produce refined channel estimates.

b: Data Normalization and Input Representation

Before training the DnCNN, each LS estimate is normalized to reduce the effect of channel magnitude variations. For the q-th training sample at relay k, the normalization

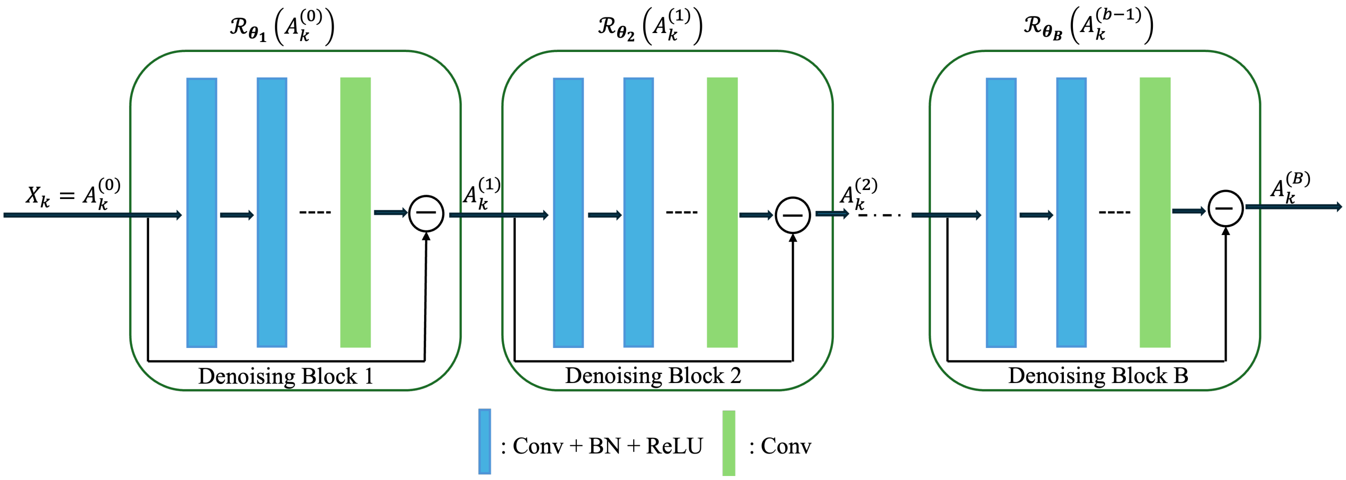

Fig. 3: Architecture of the DnCNN-based channel estimator with B cascaded residual denoising blocks.

factor is defined as

$$\eta_k^{(q)} = \sqrt{\frac{\left\|\widehat{\mathbf{h}}_{\mathrm{SS},k}^{\mathrm{LS},(q)}\right\|_2^2}{N_k}}. \tag{10}$$

The same normalization factor is used for both the LS estimate and the true channel. Thus, for the q-th training sample, the normalized input and target are given by $\widetilde{\mathbf{h}}_{\mathrm{SS},k}^{\mathrm{LS},(q)} = \widehat{\mathbf{h}}_{\mathrm{SS},k}^{\mathrm{LS},(q)}/\eta_k^{(q)}$ and $\widetilde{\mathbf{h}}_{\mathrm{SS},k}^{(q)} = \mathbf{h}_{\mathrm{SS},k}^{(q)}/\eta_k^{(q)}$, respectively. Since the channel vectors are complex-valued, while the DnCNN uses real-valued convolutional layers, each normalized channel vector is converted into a two-channel real-valued tensor. The vector is first reshaped according to the $N_{k,x} \times N_{k,y}$ URA structure, and then its real and imaginary parts are stacked as two channels. Let $\mathcal{T}(\cdot)$ denote this transformation. The input tensor and target tensor for the q-th training sample are defined as

$$\mathbf{X}_k^{(q)} = \mathcal{T}\left(\widetilde{\mathbf{h}}_{\mathrm{SS},k}^{\mathrm{LS},(q)}\right) = \left[\Re\left\{\widetilde{\mathbf{h}}_{\mathrm{SS},k}^{\mathrm{LS},(q)}\right\}, \Im\left\{\widetilde{\mathbf{h}}_{\mathrm{SS},k}^{\mathrm{LS},(q)}\right\}\right], \tag{11}$$

and

$$\mathbf{Z}_k^{(q)} = \mathcal{T}\left(\widetilde{\mathbf{h}}_{\mathrm{SS},k}^{(q)}\right) = \left[\Re\left\{\widetilde{\mathbf{h}}_{\mathrm{SS},k}^{(q)}\right\}, \Im\left\{\widetilde{\mathbf{h}}_{\mathrm{SS},k}^{(q)}\right\}\right], \tag{12}$$

where $\mathbf{X}_k^{(q)}$ is the network input and $\mathbf{Z}_k^{(q)}$ is the target output. Both tensors have size $N_{k,x} \times N_{k,y} \times 2$.

c: DnCNN Network Architecture

Fig. 3 shows the architecture of the DnCNN-based channel estimator. The network contains B cascaded residual denoising blocks. For a given input tensor $\mathbf{X}_k$, the input to the first denoising block is

$$\mathbf{A}_k^{(0)} = \mathbf{X}_k. \tag{13}$$

Each denoising block estimates the residual error in its input and subtracts it to produce a cleaner output. Let $\mathbf{A}_k^{(b-1)}$ and $\mathbf{A}_k^{(b)}$ denote the input and output of the b-th denoising block, respectively. The operation of the b-th block is written as

$$\mathbf{A}_k^{(b)} = \mathbf{A}_k^{(b-1)} - \mathcal{R}_{\boldsymbol{\theta}_b}\left(\mathbf{A}_k^{(b-1)}\right), \quad b = 1, 2, \ldots, B, \tag{14}$$

where $\mathcal{R}_{\boldsymbol{\theta}_b}(\cdot)$ is the residual mapping learned by the b-th denoising block, and $\boldsymbol{\theta}_b$ denotes its trainable parameters. As shown in Table 2, each denoising block consists of L convolutional layers, where the intermediate layers use convolution, batch normalization, and ReLU activation, while the final layer uses convolution to estimate the residual error. For layer ℓ, F_ℓ denotes the number of convolutional filters, and S_ℓ denotes the convolutional kernel size, expressed as spatial height $\times$ spatial width $\times$ number of input channels. By repeating this operation through B denoising blocks, the network progressively removes the residual estimation error from the LS-based input. The overall mapping of the cascaded denoising network is expressed as

$$g_{\boldsymbol{\theta}}\left(\mathbf{X}_k\right) = \mathbf{X}_k - \sum_{b=1}^{B} \mathcal{R}_{\boldsymbol{\theta}_b}\left(\mathbf{A}_k^{(b-1)}\right), \tag{15}$$

where $\boldsymbol{\theta} = \{\boldsymbol{\theta}_1, \boldsymbol{\theta}_2, \ldots, \boldsymbol{\theta}_B\}$ represents the trainable parameters of all denoising blocks. The output tensor of the network is given by

$$\widehat{\mathbf{Z}}_k = \mathbf{A}_k^{(B)} = g_{\boldsymbol{\theta}}\left(\mathbf{X}_k\right). \tag{16}$$

d: Training Objective

During training, the network output $\widehat{\mathbf{Z}}_k^{(q)} = g_{\boldsymbol{\theta}}(\mathbf{X}_k^{(q)})$ is compared with the corresponding target tensor $\mathbf{Z}_k^{(q)}$. To compute the loss in the normalized complex-valued channel domain, the estimated tensor is mapped back using the inverse transformation $\mathcal{M}(\cdot)$ as

$$\widetilde{\mathbf{h}}_{\mathrm{SS},k}^{\mathrm{DnCNN},(q)} = \mathcal{M}\left(\widehat{\mathbf{Z}}_k^{(q)}\right). \tag{17}$$

The network parameters are optimized by minimizing the sample-wise NMSE between the normalized true

Table 2: Structure of one denoising block.

Layer	Operation	Filters	Kernel
$\ell = 1$	Conv+BN+ReLU	F_1	S_1
$\ell = 2, \ldots, L-1$	Conv+BN+ReLU	F_ℓ	S_ℓ
$\ell = L$	Conv	F_L	S_L

Conv, BN, and ReLU denote convolution, batch normalization, and rectified linear unit activation, respectively.

channel $\widetilde{\mathbf{h}}_{\mathrm{SS},k}^{(q)}$ and the DnCNN-estimated channel, which is defined as

$$\mathcal{J}_{\mathrm{NMSE}} = \frac{1}{Q}\sum_{q=1}^{Q} \frac{\left\|\widetilde{\mathbf{h}}_{\mathrm{SS},k}^{(q)} - \widetilde{\mathbf{h}}_{\mathrm{SS},k}^{\mathrm{DnCNN},(q)}\right\|_2^2}{\left\|\widetilde{\mathbf{h}}_{\mathrm{SS},k}^{(q)}\right\|_2^2}. \tag{18}$$

Accordingly, the optimal network parameters are obtained as $\boldsymbol{\theta}^\star = \arg\min_{\boldsymbol{\theta}} \mathcal{J}_{\mathrm{NMSE}}(\boldsymbol{\theta})$, where $\boldsymbol{\theta}^\star$ denotes the trained DnCNN parameters used during online estimation.

e: Online Estimation

During online estimation, relay k receives the new pilot signal $\dot{\mathbf{Y}}_k$ and obtains the LS estimate using (6). The LS estimate is then normalized using the normalization factor η_k in (10) and converted into the two-channel input tensor $\dot{\mathbf{X}}_k \in \mathbb{R}^{N_{k,x}\times N_{k,y}\times 2}$. The trained DnCNN model with parameters $\boldsymbol{\theta}^\star$ produces the normalized tensor-domain output $g_{\boldsymbol{\theta}^\star}(\dot{\mathbf{X}}_k)$. This output is then converted back to the complex-valued channel domain using the inverse transformation $\mathcal{M}(\cdot)$ and denormalized to obtain the final channel estimate as

$$\widehat{\mathbf{h}}_{\mathrm{SS},k}^{\mathrm{DnCNN}} = \eta_k \mathcal{M}\left(g_{\boldsymbol{\theta}^\star}\left(\dot{\mathbf{X}}_k\right)\right). \tag{19}$$

The resulting channel estimate is then used in the relay-selection stage, which is discussed in the following section.

B. Relay Selection

After channel estimation, the SS selects one relay from the relay set $\mathcal{K}$ to forward its data to the BS. The SS–relay channels are estimated from pilot transmission, as discussed in the previous section. The relay–BS CSI is assumed to be available because this work focuses on the effect of SS–relay channel-estimation errors on relay-selection performance. This assumption avoids additional uncertainty from the second-hop links. It also allows us to evaluate the best achievable performance of the proposed framework under accurate relay–BS CSI. Based on this setup, two relay-selection methods are considered in this section. Both methods use the estimated SS–relay data rate, denoted by $\widehat{R}_{\mathrm{SS},k}$. For each relay k, $\widehat{R}_{\mathrm{SS},k}$ is defined as

$$\widehat{R}_{\mathrm{SS},k} = W_{\mathrm{SS},k}\log_2\left(1+\widehat{\gamma}_{\mathrm{SS},k}\right), \tag{20}$$

where $\widehat{\gamma}_{\mathrm{SS},k}$ is the estimated received SNR at relay k. Based on the estimated channel $\widehat{\mathbf{h}}_{\mathrm{SS},k}$, the estimated SNR $\widehat{\gamma}_{\mathrm{SS},k}$ is computed as

$$\widehat{\gamma}_{\mathrm{SS},k} = \frac{P_{\mathrm{SS}}\left|\widehat{\mathbf{w}}_k^H\widehat{\mathbf{h}}_{\mathrm{SS},k}\right|^2}{\sigma_k^2}, \tag{21}$$

where P_{SS} is the transmit power of the SS, and $\widehat{\mathbf{w}}_k$ is the maximum ratio combining (MRC) combining vector given by $\widehat{\mathbf{w}}_k = \widehat{\mathbf{h}}_{\mathrm{SS},k}/\|\widehat{\mathbf{h}}_{\mathrm{SS},k}\|_2$.

1) Method 1: Partial Relay Selection

Method 1 follows the partial relay-selection principle [34], where relay selection is performed using only $\widehat{R}_{\mathrm{SS},k}$. Accordingly, the selected relay is obtained as

$$k_1^\star = \arg\max_{k\in\mathcal{K}} \widehat{R}_{\mathrm{SS},k}. \tag{22}$$

After obtaining $k_1^\star$, the achieved end-to-end data rate of Method 1 is evaluated as

$$R_1^{\mathrm{ach}} = \frac{1}{2}\min\left(\widetilde{R}_{\mathrm{SS},k_1^\star}, R_{k_1^\star,\mathrm{BS}}\right), \tag{23}$$

where $R_{k_1^\star,\mathrm{BS}}$ is the data rate of the relay $k_1^\star$–BS link, and $\widetilde{R}_{\mathrm{SS},k_1^\star}$ denotes the achieved data rate of the SS–relay $k_1^\star$ link. The $\widetilde{R}_{\mathrm{SS},k_1^\star}$ is defined as

$$\widetilde{R}_{\mathrm{SS},k_1^\star} = W_{\mathrm{SS},k_1^\star}\log_2\left(1+\widetilde{\gamma}_{\mathrm{SS},k_1^\star}\right). \tag{24}$$

where $W_{\mathrm{SS},k_1^\star}$ is the bandwidth of the SS–relay $k_1^\star$ link, and $\widetilde{\gamma}_{\mathrm{SS},k_1^\star}$ is the achieved received SNR at relay $k_1^\star$. For performance evaluation, $\widetilde{\gamma}_{\mathrm{SS},k_1^\star}$ is calculated using the true channel realization while keeping the combining vector obtained from the estimated channel as

$$\widetilde{\gamma}_{\mathrm{SS},k_1^\star} = \frac{P_{\mathrm{SS}}\left|\widehat{\mathbf{w}}_{k_1^\star}^H\mathbf{h}_{\mathrm{SS},k_1^\star}\right|^2}{\sigma_{k_1^\star}^2}, \tag{25}$$

where $\mathbf{h}_{\mathrm{SS},k_1^\star}$ is the true channel realization corresponding to $k_1^\star$, $\widehat{\mathbf{w}}_{k_1^\star}$ is obtained from $\widehat{\mathbf{h}}_{\mathrm{SS},k_1^\star}$, and $\sigma_{k_1^\star}^2$ is the noise power at relay $k_1^\star$.

2) Method 2: End-to-End Rate-Based Relay Selection

Method 2 considers both $\widehat{R}_{\mathrm{SS},k}$ and $R_{k,\mathrm{BS}}$ during relay selection. For relay k, the estimated end-to-end data rate is defined as

$$\widehat{R}_k^{\mathrm{E2E}} = \frac{1}{2}\min\left(\widehat{R}_{\mathrm{SS},k}, R_{k,\mathrm{BS}}\right). \tag{26}$$

Then, the selected relay is obtained as

$$k_2^\star = \arg\max_{k\in\mathcal{K}} \widehat{R}_k^{\mathrm{E2E}}. \tag{27}$$

After obtaining $k_2^\star$, the achieved end-to-end data rate of Method 2 is evaluated as

$$R_2^{\mathrm{ach}} = \frac{1}{2}\min\left(\widetilde{R}_{\mathrm{SS},k_2^\star}, R_{k_2^\star,\mathrm{BS}}\right), \tag{28}$$

where $R_{k_2^\star,\mathrm{BS}}$ is the data rate of the relay $k_2^\star$–BS link, and $\widetilde{R}_{\mathrm{SS},k_2^\star}$ denotes the achieved data rate of the SS–relay $k_2^\star$ link. The $\widetilde{R}_{\mathrm{SS},k_2^\star}$ is defined as

$$\widetilde{R}_{\mathrm{SS},k_2^\star} = W_{\mathrm{SS},k_2^\star} \log_2\left(1 + \widetilde{\gamma}_{\mathrm{SS},k_2^\star}\right). \tag{29}$$

where $W_{\mathrm{SS},k_2^\star}$ is the bandwidth of the SS–relay $k_2^\star$ link, and $\widetilde{\gamma}_{\mathrm{SS},k_2^\star}$ is the achieved received SNR at relay $k_2^\star$. Similar to Method 1, $\widetilde{\gamma}_{\mathrm{SS},k_2^\star}$ is calculated using the true channel realization while keeping the combining vector obtained from the estimated channel as

$$\widetilde{\gamma}_{\mathrm{SS},k_2^\star} = \frac{P_{\mathrm{SS}} \left| \widehat{\mathbf{w}}_{k_2^\star}^H \mathbf{h}_{\mathrm{SS},k_2^\star} \right|^2}{\sigma_{k_2^\star}^2}, \tag{30}$$

where $\mathbf{h}_{\mathrm{SS},k_2^\star}$ is the true channel realization corresponding to $k_2^\star$, $\widehat{\mathbf{w}}_{k_2^\star}$ is obtained from $\widehat{\mathbf{h}}_{\mathrm{SS},k_2^\star}$, and $\sigma_{k_2^\star}^2$ is the noise power at relay $k_2^\star$.

Computational Complexity: The proposed methodology consists of offline and online processing stages. In the offline stage, the pilot pseudoinverse and the LMMSE filtering matrix are computed, while the DnCNN model is trained using the generated channel datasets. These operations are performed in advance and are not repeated during real-time channel estimation. In the online stage, a new channel estimate is obtained from the received pilot signal using the trained or precomputed estimator. Therefore, the online computational complexities of the LS, LMMSE, and DnCNN-based estimators are $\mathcal{O}(N_k C)$, $\mathcal{O}(N_k^2 + N_k C)$, and $\mathcal{O}\left(N_k C + B N_k \sum_{\ell=1}^{L} s_\ell^2 n_{\ell-1} n_\ell\right)$, respectively. Here, $n_{\ell-1}$ and n_ℓ denote the numbers of input and output feature maps in layer ℓ.

V. Simulation Results

This section analyzes the performance of the DnCNN-based channel estimation and relay-selection approach for the considered maritime relay-assisted SAGSIN. The simulations are carried out in a three-dimensional maritime coordinate system. The coastline is aligned with the y-axis, the x-axis points toward the sea, and the z-axis represents the height above the sea surface. The SS location is randomly generated within a rectangular maritime service area, where the offshore coordinate is uniformly distributed as $x_{\mathrm{SS}} \in [x_{\min}, x_{\max}]$ and the along-coast coordinate is uniformly distributed as $y_{\mathrm{SS}} \in [y_{\min}, y_{\max}]$. Since the SS is located on the sea surface, its height is fixed as $z_{\mathrm{SS}} = h_{\mathrm{SS}}$. The relay locations are fixed in the same three-dimensional coordinate system according to their deployment heights and distances from the coastline. The default simulation parameters are summarized in Table 3. For each relay link, 50,000 unique SS locations are generated, and the same set of locations is used at all five transmit-power values to provide a fair comparison across different power levels. Then, the total dataset contains 250,000 Monte Carlo realizations over all transmit-power values for each relay link. For each relay, 80% of the generated samples are used for training, 10% are used for validation, and the remaining 10% are used for testing. Separate DnCNN models are trained for the SS–OS, SS–HAP, and SS–SAT links. The dataset is divided according to the SS-location index, where all samples generated from the same location at different

Table 3: Simulation parameters [1], [3], [12], [35]–[40]

Notation	Values
f_k	$\begin{cases} 2.4\ \text{GHz}, & k = \text{OS}, \\ 2\ \text{GHz}, & k = \text{HAP}, \\ 6\ \text{GHz}, & k = \text{SAT}. \end{cases}$
x_{BS}	0 m
x_k	$\begin{cases} 1000\ \text{m}, & k = \text{OS}, \\ 2000\ \text{m}, & k = \text{HAP}, \\ 2000\ \text{m}, & k = \text{SAT} \end{cases}$
y_{BS}, y_k	0 m, $\quad k \in \mathcal{K}$
h_{BS}	20 m
D_k	$\lambda_k/2, \quad k \in \mathcal{K}$
$x_{\min}, x_{\max}$	1 km, 300 km
$y_{\min}, y_{\max}$	-1 km, 1 km
$N_{k,x} \times N_{k,y}$	8×8 ($N_k = 64$)
$N_{\mathrm{BS},x} \times N_{\mathrm{BS},y}$	8×8 ($N_{\mathrm{BS}} = 64$)
C	$\{8, 16, 32, 48, 64\}$ symbols
h_{SS}	1 m
h_k	$\begin{cases} 20\ \text{m}, & k = \text{OS}, \\ 22 \times 10^3\ \text{m}, & k = \text{HAP}, \\ 550 \times 10^3\ \text{m}, & k = \text{SAT} \end{cases}$
G_{SS}	10 dBi
G_k	$\begin{cases} 30\ \text{dBi}, & k = \text{OS}, \\ 20\ \text{dBi}, & k = \text{HAP}, \\ 41\ \text{dBi}, & k = \text{SAT} \end{cases}$
$W_{\mathrm{SS},k}$	$\begin{cases} 20\ \text{MHz}, & k = \text{OS}, \\ 20\ \text{MHz}, & k = \text{HAP}, \\ 36\ \text{MHz}, & k = \text{SAT} \end{cases}$
$W_{k,\mathrm{BS}}$	$\begin{cases} 20\ \text{MHz}, & k = \text{OS}, \\ 20\ \text{MHz}, & k = \text{HAP}, \\ 36\ \text{MHz}, & k = \text{SAT} \end{cases}$
N_0	-160 dBm/Hz
$K_{\mathrm{SS},k}$	10 dB
P_{SS}	$\{20, 25, 30, 35, 40\}$ dBm
P_k	$\begin{cases} 30\ \text{dBm}, & k = \text{OS}, \\ 45\ \text{dBm}, & k = \text{HAP}, \\ 60\ \text{dBm}, & k = \text{SAT} \end{cases}$
$\tilde{r}_k$	$\mathcal{N}(2.6, 1.63)$
F_1, F_ℓ, F_L	64, 64, 2
S_1, S_ℓ, S_L	$3 \times 3 \times 2$, $3 \times 3 \times 64$, $3 \times 3 \times 64$

transmit-power values are kept in the same training, validation, or test partition to avoid location-based data leakage. The DnCNN models consist of $B = 3$ cascaded denoising blocks, where each block contains $L = 4$ layers. The DnCNN models are trained offline using the Adam optimizer with an initial learning rate of 10^{-3}, a batch size of 64. Training is performed for a maximum of 100 epochs, while early stopping is applied if the validation loss does not improve for 10 consecutive epochs. The learning rate is reduced by a factor of 0.5 when the validation loss does not improve for five epochs, and the model with the lowest validation loss is retained for testing.

The simulation results are presented in the following subsections. First, the channel estimation accuracy of LS, LMMSE, and the DnCNN-based estimator is compared using NMSE. Then, the achieved end-to-end data rate is analyzed to show how channel estimation accuracy affects relay selection and overall system performance. The end-to-end outage probability is also evaluated to compare the reliability of relay selection using perfect CSI, random relay selection, and the LS, LMMSE, and DnCNN-based channel estimates. Finally, the relay selection probability is examined as the SS moves away from the coastline, which illustrates how the preferred relay changes with the SS location.

A. Ablation Study of the DnCNN Architecture

Fig. 4 shows the effect of the number of convolutional layers on the NMSE performance of the adapted DnCNN-based estimator. The models with L=2, 4, 8, and 16 convolutional layers per denoising block are compared. Similar performance trends are observed for the OS, HAP, and SAT links. The models with L=4 and L=8 generally provide the best and nearly identical NMSE performance. However, increasing the number of layers beyond L=4 does not provide a significant improvement. Therefore, L=4 is selected to reduce the computational complexity while maintaining good estimation accuracy. Fig. 5 shows the effect of the number of denoising blocks. The models with B=2, 3, and 4 are evaluated using L=4. The model with B=3 achieves the lowest NMSE for the OS link and provides performance comparable to the other models for the HAP and SAT links. Therefore, B=3 is selected as an appropriate trade-off between estimation accuracy and computational complexity. Fig. 6 compares the selected adapted DnCNN model with a conventional convolutional neural network (CNN) model for all three links. The adapted DnCNN model achieves better NMSE performance for the SS–OS, SS–HAP, and SS–SAT links.

B. NMSE Versus Transmit Power

Fig. 7 shows the NMSE performance of the LS, LMMSE, and the DnCNN-based estimators for the OS, HAP, and SAT links under different SS transmit powers. The NMSE of all estimators decreases as the transmit power increases. This is because a higher transmit power improves the received pilot signal quality at the relay, thereby reducing the effect of noise on the channel estimation process. The performance of the LS and LMMSE estimators is first considered. Among them, LS provides the weakest estimation performance, particularly at low transmit power. This is mainly because LS estimates the channel directly from the received pilot observations without exploiting any prior statistical information about the channel. In contrast, LMMSE generally improves the estimation accuracy by incorporating second-order channel statistics through the channel covariance matrix. This improvement is clearly observed for the HAP and SAT links. However, for the OS link, LMMSE provides only a marginal gain over LS. This can be attributed to the two-ray Rician propagation characteristics of the SS–OS link, where the received signal is affected by both the direct path and the sea-surface-reflected path. As a result, the remaining estimation error cannot be fully suppressed by a linear estimator that relies mainly on second-order statistical information.

The adapted DnCNN-based estimator is then compared with the LMMSE estimator. For the OS, HAP, and SAT links, the DnCNN-based estimator generally provides the lowest NMSE at low and medium transmit powers. The improvement is most noticeable in the low transmit power regime, where the received pilot observations are strongly affected by noise. This improvement is achieved because the adapted DnCNN-based estimator adopts a nonlinear denoising structure and learns to recover a cleaner channel estimate from noisy LS-based training examples, whereas LMMSE is limited to a linear estimation framework based on second-order channel statistics. As the transmit power increases, the received pilot signals become less noisy, and the performance gap between LMMSE and the DnCNN-based estimator becomes smaller for some links. Nevertheless, the DnCNN-based estimator still provides the lowest NMSE for the OS and HAP links at high transmit power. For the SAT link at high transmit power, LMMSE slightly outperforms the DnCNN-based estimator, indicating that the two estimators provide comparable performance in this operating regime. Overall, these results show that the adapted DnCNN-based estimator provides reliable channel estimation performance for heterogeneous maritime relay links, with the most significant improvement obtained under low-transmit-power conditions.

C. NMSE Versus Pilot Sequence Length

Fig. 8 shows the effect of the pilot sequence length on the NMSE performance when $P_{\mathrm{SS}} = 30$ dBm. The NMSE of all estimators generally decreases as the pilot sequence length C increases. This is because a longer pilot sequence provides more received observations for

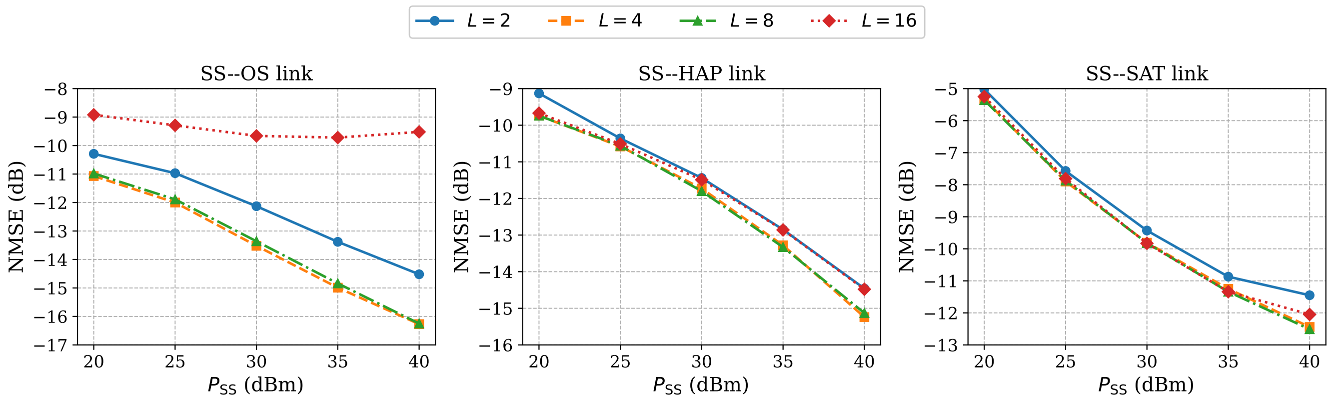

Fig. 4: NMSE performance of the adapted DnCNN-based channel estimator with different numbers of convolutional layers for the SS–OS, SS–HAP, and SS–SAT links, where $B = 3$.

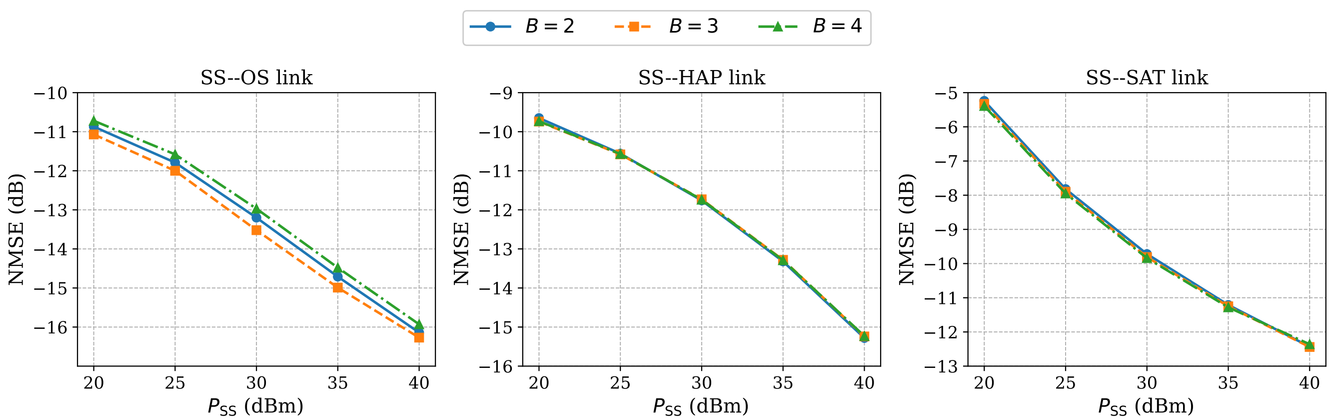

Fig. 5: NMSE performance of the adapted DnCNN-based channel estimator with different numbers of denoising blocks for the SS–OS, SS–HAP, and SS–SAT links, where $L = 4$.

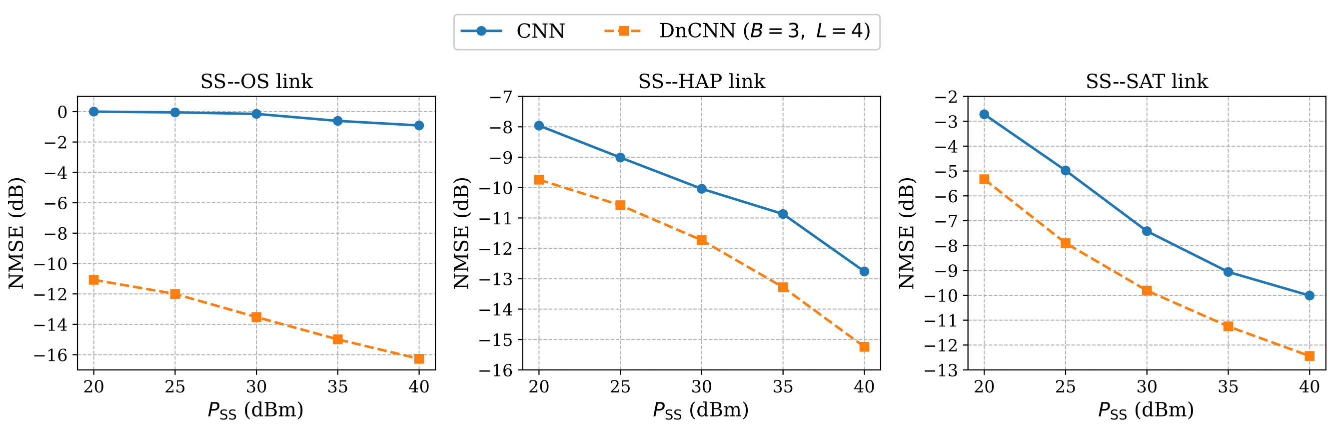

Fig. 6: NMSE performance comparison between the CNN-based and DnCNN-based channel estimators for the SS–OS, SS–HAP, and SS–SAT links.

channel estimation, which reduces the impact of noise on the estimated channel.

The performance of the LS and LMMSE estimators is first considered. Among them, LS gives the weakest estimation performance for all relay links, particularly

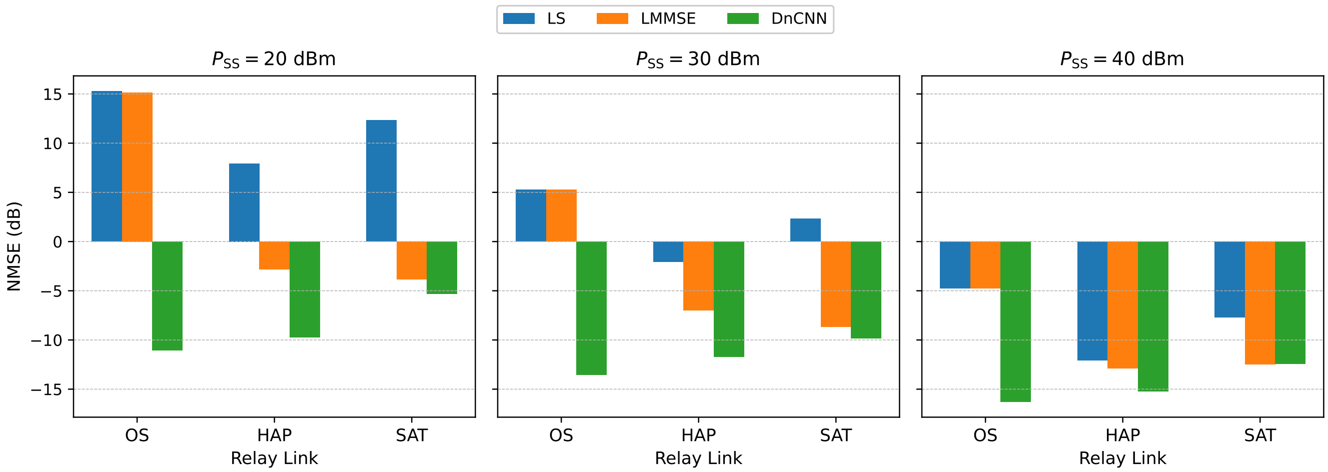

Fig. 7: NMSE performance of LS, LMMSE, and DnCNN-based channel estimation for the OS, HAP, and SAT links at low, medium, and high SS transmit powers with $C = 32$.

when the pilot sequence length is short. This is because LS estimates the channel directly from the received pilot observations without using prior channel statistical information, making it more sensitive to noise when limited pilot observations are available. In contrast, LMMSE achieves better NMSE performance than LS by exploiting second-order channel statistics through the channel covariance matrix. This improvement is especially clear for the HAP and SAT links. However, for the OS link, the gain of LMMSE over LS is relatively small, which is consistent with the transmit-power-based results.

The DnCNN-based estimator further improves the NMSE performance compared with LMMSE and achieves the lowest NMSE for all relay links over the considered pilot sequence lengths. The improvement is more noticeable when C is small, since the initial LS estimate contains stronger residual noise under limited pilot observations. As C increases, the received pilot observations become more informative, and the performance gap between LMMSE and the DnCNN estimator becomes smaller for some links. Overall, these results show that the DnCNN-based estimator remains effective under different pilot sequence lengths and provides reliable channel estimation performance for the considered maritime relay links.

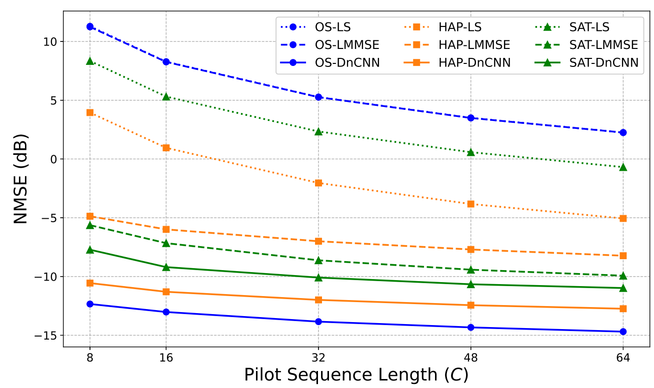

Fig. 8: NMSE performance versus pilot length for the OS, HAP, and SAT links when $P_{SS} = 30$ dBm.

D. Achieved End-to-End Data Rate Versus SS Transmit Power

Fig. 9 shows the average achieved end-to-end data rate versus the SS transmit power. The transmit power is varied from 20 dBm to 35 dBm. The figure presents the Method 1 results obtained using the LS, LMMSE, and adapted DnCNN channel estimates. Method 2 is also evaluated using the adapted DnCNN channel estimates. The results are compared with perfect CSI and random relay selection. Perfect CSI is used as the upper-bound benchmark because it selects the relay using the true channel information. Random relay selection is used as the lower-bound benchmark because it selects the relay without using channel information. Among the considered estimators, the adapted DnCNN-based relay selection achieves a higher end-to-end data rate than the LS- and LMMSE-based relay selection, particularly at lower transmit powers. The DnCNN-based methods achieve data rates close to perfect CSI and clearly outperform random relay selection over the whole transmit-power range. Using perfect CSI as the reference, the gap between the adapted DnCNN-based method and perfect CSI is about 7.83% at low transmit power. This gap decreases to about 4.59% at medium transmit power and 3.11% at high transmit power. This happens because higher transmit power improves the received pilot quality and reduces the channel-estimation error. Therefore, the adapted DnCNN-based method can make relay-selection decisions closer to the perfect CSI case.

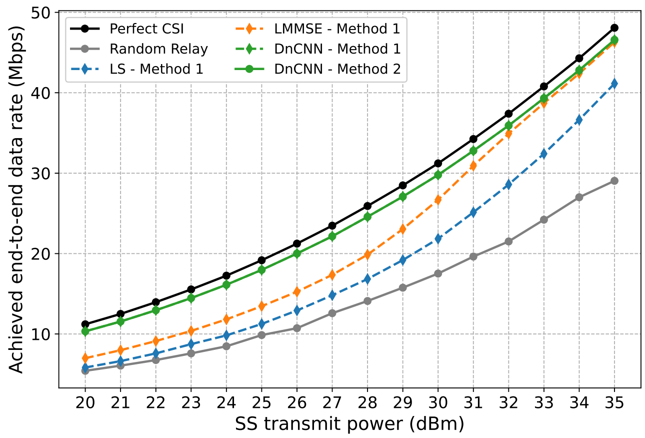

Fig. 9: Average achieved end-to-end data rate versus SS transmit power for different relay selection methods.

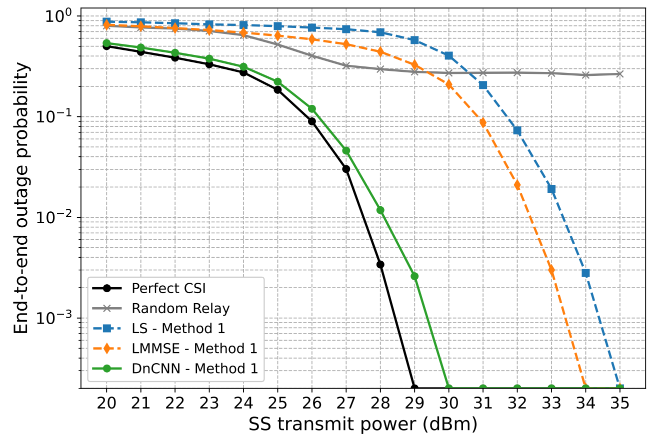

Fig. 10: End-to-end outage probability versus SS transmit power for perfect CSI, random relay selection, and LS, LMMSE, and DnCNN-based relay selection.

In addition to the benchmark comparison, Fig. 9 shows that the two proposed DnCNN-based relay selection methods have almost the same performance. Their curves overlap because the SS–relay k link is usually the bottleneck in the considered setup. Therefore, selecting the relay based on the estimated first-hop rate gives almost the same decision as selecting the relay based on the estimated end-to end rate. As a result, both proposed methods achieve almost the same end-to-end data rate.

E. End-to-End Outage Probability Versus Sea-Surface Station Transmit Power

For the selected relay k, the achieved end-to-end SINR is determined by the weaker hop as

$$\gamma_{\text{e2e}}^{\text{ach}} = \min\left(\gamma_{\text{SS-}k}^{\text{ach}}, \gamma_{k\text{-BS}}\right). \tag{31}$$

Accordingly, the outage probability is defined as

$$P_{\text{out}} = \Pr\left(\gamma_{\text{e2e}}^{\text{ach}} \leq \gamma_{\text{th}}\right). \tag{32}$$

Following the reference work [1], the decoding threshold is set to $\gamma_{\text{th}} = -5$ dB. Fig. 10 shows the end-to-end outage probability versus the SS transmit power for Method 1 relay selection. Perfect CSI provides the lowest outage probability because the relay is selected using the true channel information. Among the channel-estimation-based methods, the DnCNN-based method achieves a lower outage probability than the LS- and LMMSE-based methods. This is because its more accurate channel estimates result in more reliable relay selection and improved receive combining. The outage probability of the channel-aware methods decreases as the SS transmit power increases because the first-hop received SNR and channel-estimation accuracy improve. In contrast, random relay selection has a higher outage probability because it does not consider the channel conditions when selecting the relay.

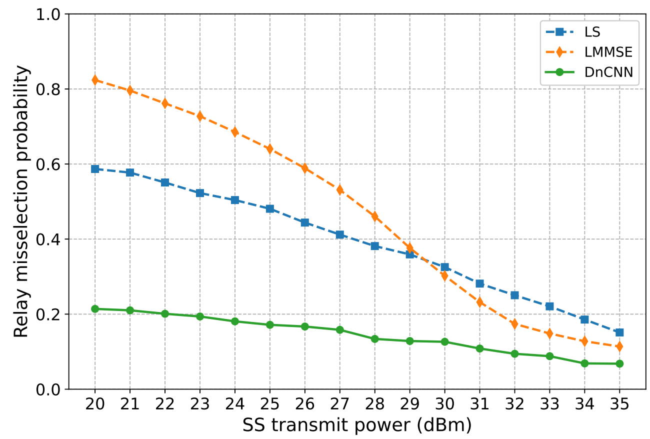

Fig. 11: Relay misselection probability versus SS transmit power for Method 1 using the LS, LMMSE, and adapted DnCNN channel estimates.

F. Misselection Probability Versus SS Transmit Power

Fig. 11 shows the relay misselection probability versus the SS transmit power. The misselection probability decreases as the transmit power increases. This is because the received pilot signal becomes stronger. As a result, the channel estimates become more accurate.The adapted DnCNN-based method achieves the lowest misselection probability over the entire transmit-power range. Therefore, it selects the same relay as the perfect-CSI benchmark more often.

Although LMMSE provides better channel-estimation accuracy than LS, it applies stronger filtering at low transmit power. This can change the ordering of the estimated relay-link rates. Therefore, the LMMSE-based method can have a higher misselection probability at low transmit power. As the transmit power increases, this effect becomes smaller and the LMMSE-based relay selection improves.

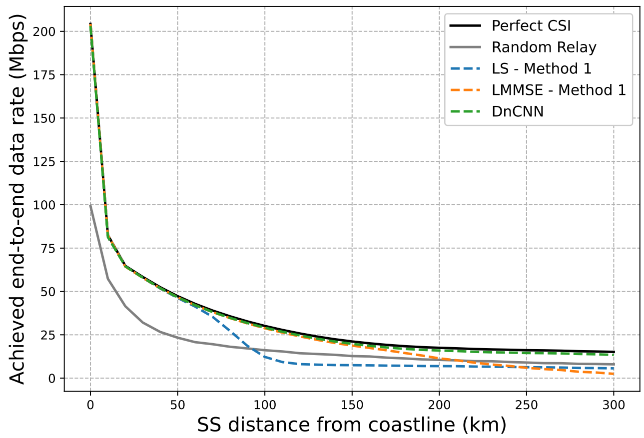

Fig. 12: Average achieved end-to-end data rate versus SS distance for perfect CSI, random relay selection, and Method 1 using the LS, LMMSE, and DnCNN-based channel estimates

.

G. Achieved End-to-End Data Rate Versus SS Distance

Fig. 12 shows the average achieved end-to-end data rate versus the SS distance. This comparison considers perfect CSI, random relay selection, and Method 1 using the LS, LMMSE, and DnCNN-based channel estimates. Only Method 1 is shown because Fig. 9 showed that Method 1 and Method 2 give almost identical performance. The data rate decreases as the SS moves farther from the coastal region. This happens because the propagation distance becomes longer, which increases path loss and reduces the received signal power at the relays. As a result, the first-hop rate decreases and limits the end-to-end rate. Perfect CSI gives the highest data rate because it selects the relay using true channel information, while random relay selection gives the lowest performance because it does not use channel information. Among the channel-estimation-based methods, the DnCNN-based method achieves the closest performance to perfect CSI and generally outperforms the LS- and LMMSE-based methods. This improvement is consistent with the better channel-estimation accuracy provided by the DnCNN estimator. The DnCNN-based method closely follows the perfect CSI curve, especially at short and medium distances, and clearly outperforms random relay selection over the whole distance range. At larger distances, the gap between perfect CSI and the DnCNN-based method slightly increases because weaker received pilot signals make channel estimation more difficult. These results show that the DnCNN-based estimator can support reliable channel-aware relay selection in distance-dependent maritime communication scenarios.

H. Relay Selection Probability Versus SS Distance

Figs. 13a–13c show the relay selection probability versus the SS distance for Method 1 using the DnCNN, LS, and LMMSE channel estimates, respectively, together with the perfect-CSI and random relay-selection benchmarks. The selected relay changes as the SS moves away from the coastline. At short distances, perfect CSI mainly selects the OS, since the SS–OS link is strong near the coastal region. As the distance increases, the SS–OS link becomes weaker, and the HAP is selected more often at medium distances. At longer distances, the SAT becomes the preferred relay because it can provide wider offshore coverage. This trend shows that the best relay depends strongly on the SS location and the corresponding link quality.

The DnCNN-based method follows a relay selection trend similar to perfect CSI. This shows that the DnCNN estimator can provide useful channel information for relay selection. Small differences between the two methods appear because the DnCNN method uses estimated channel information, whereas perfect CSI uses the true channel information. These differences are more visible near the relay transition regions, where two relay candidates may have similar data rates. In contrast, random relay selection gives almost constant selection probabilities for the three relays because it does not use channel information. These results confirm that the DnCNN-based method can make channel-aware relay selection decisions and closely follow the perfect CSI benchmark.

VI. Conclusion and Future Research Directions

This paper investigated channel estimation and relay selection for a maritime SAGSIN, where an SS communicates with a BS through one selected relay among an OS, a HAP, and a SAT. Since these relay candidates operate in different propagation environments, the quality of the estimated channel between the SS and the relay k directly affects relay selection and the resulting end-to-end data rate. To address this issue, three channel estimation methods were considered for the SS–relay k links: LS, LMMSE, and a DnCNN-based estimator. The estimated channels were then used in two relay-selection strategies based on the estimated first-hop data rate and the estimated end-to-end data rate.

Simulation results showed that the DnCNN-based estimator can significantly improve channel estimation accuracy compared with the traditional LS estimator and can outperform the LMMSE estimator in most considered scenarios. The gain of the DnCNN-based estimator was especially noticeable under challenging conditions, such as low transmit power and short pilot length, where the LS estimate contains stronger noise-induced estimation errors. These results demonstrate the effectiveness of learning-based residual denoising for improving pilot-

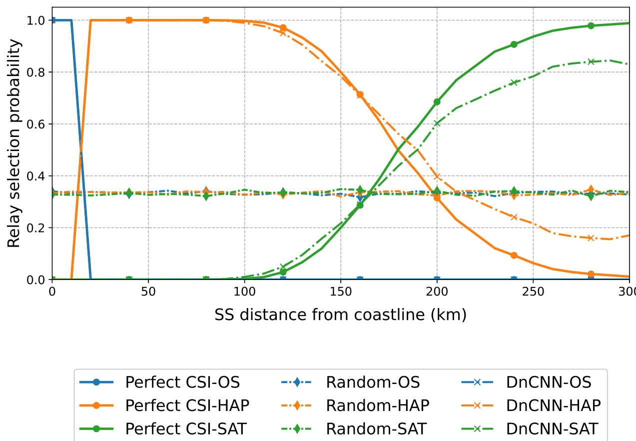

(a) DnCNN-based relay selection.

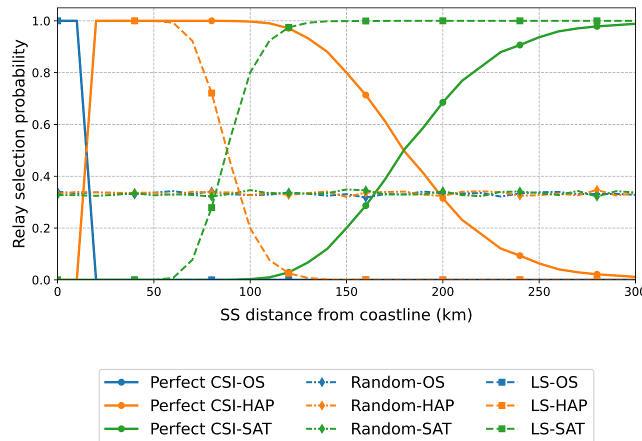

(b) LS-based relay selection.

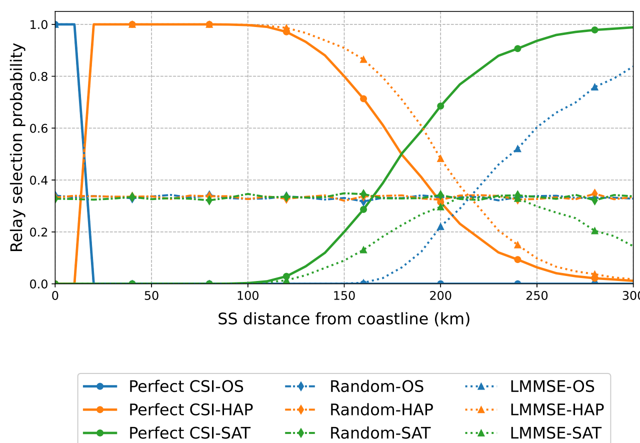

(c) LMMSE-based relay selection.

Fig. 13: Relay selection probability versus SS distance for perfect CSI, random relay selection, and the considered channel-estimation-based relay-selection methods: (a) DnCNN, (b) LS, and (c) LMMSE.

based channel estimation in heterogeneous maritime links.

The results further showed that improved channel estimation leads to more reliable relay selection. In particular, the DnCNN achieved an end-to-end data rate and outage probability close to the perfect-CSI benchmark and clearly outperformed random relay selection. This confirms that accurate channel estimation is important not only for estimating the channel itself, but also for improving the overall communication performance of maritime relay-assisted SAGSINs. Therefore, the proposed framework can support more reliable connectivity for maritime applications such as ship communication, offshore platforms, coastal monitoring, and emergency services.

Moreover, we will investigate the effects of imperfect and outdated CSI on both the SS–relay and relay–BS links. We will also study how channel variations, channel aging, and processing or feedback delays affect relay selection, end-to-end data rate, and outage probability. In addition, the channel model will be extended to include more detailed maritime propagation effects, such as residual Doppler, platform altitude variations, atmospheric absorption, shadowing, sea-state-dependent reflections, and time-varying rain attenuation.

Acknowledgment

This work was supported in part by the Canada Excellence Research Chair (CERC) Program CERC-2022-00109 and in part by the Natural Sciences and Engineering Research Council of Canada (NSERC) Discovery Grant Program RGPIN-2025-04941. The work of O. A. Dobre was supported in part by the Canada Research Chairs (CRC) Program CRC-2022-00187, Canada First Research Excellence Fund (CFREF) Transforming Climate Action, Grant TCA-LRP-20241-MUN-1.3-03, and in part by CFREF Clean Arctic Shipping Initiative, Grant CFREF-2022-00062.

References

[1] J. Xu, M. A. Kishk, and M.-S. Alouini, "Space-air-ground-sea integrated networks: Modeling and coverage analysis," *IEEE Trans. Wirel. Commun.*, vol. 22, no. 9, pp. 6298–6313, Sep. 2023.

[2] H. Guo, J. Li, J. Liu, N. Tian, and N. Kato, "A survey on space-air-ground-sea integrated network security in 6G," *IEEE Commun. Surv. Tutor.*, vol. 24, no. 1, pp. 53–87, 1st Quart. 2022.

[3] Z. Zhou, X. Chen, M. Ying, Z. Yang, C. Huang, Y. Cai, and Z. Zhang, "Unified design of space-air-ground-sea integrated maritime communications," *IEEE Trans. Commun.*, vol. 73, no. 12, pp. 13 441–13 455, Dec. 2025.

[4] J. Zhang, Q. Li, K. Fang, Z. Wang, D. Zhang, H. Li, and B. Clerckx, "Spherical stacked intelligent metasurfaces: A paradigm for full-space wave-domain processing," *IEEE Commun. Mag.*, pp. 1–8, early access 2026.

[5] A. Wei, Z. Wang, K. Fang, J. Zhang, Y. Dong, L. Yang, and Q. Li, "Near-field beam training design for stacked intelligent metasurface assisted communication systems," *IEEE Trans. Veh. Technol.*, pp. 1–6, early access 2026.

[6] Q. Li, M. El-Hajjar, C. Xu, J. An, C. Yuen, and L. Hanzo, "Stacked intelligent metasurface-based transceiver design for near-field wideband systems," *IEEE Trans. Commun.*, vol. 73, no. 9, pp. 8125–8139, Sep. 2025.

[7] C. Zhang, Q. Li, C. Xu, L.-L. Yang, and L. Hanzo, "Space-air-ground integrated networks: Their channel model and performance analysis," *IEEE Open J. Veh. Technol.*, vol. 6, pp. 1501–1523, May 2025.

[8] B. He, P. Tang, P. Liu, Z. Ding, P. Peng, and J. Zhang, "Channel measurement and modelling in nearshore scenarios for air-sea communications," in *IEEE 5th Int. Conf. Elect. Circuits and Info. Eng. (ECIE), Guangzhou, China*, May 2025, pp. 127–132.

[9] A. P. Millar, S. Weiss, and R. W. Stewart, "Training-based channel estimation algorithms for dual hop MIMO OFDM relay systems," *IEEE Trans. Commun.*, vol. 63, no. 12, pp. 4711–4726, Dec. 2015.

[10] A. Liao, Z. Gao, D. Wang, H. Wang, H. Yin, D. W. K. Ng, and M.-S. Alouini, "Terahertz ultra-massive MIMO-based aeronautical communications in space-air-ground integrated networks," *IEEE J. Sel. Areas Commun.*, vol. 39, no. 6, pp. 1741–1767, Jun. 2021.

[11] J. Zhao, Y. Zhu, K. Cai, Z. Gao, Z. Han, and L. Hanzo, "Multiple-antenna aided aeronautical communications in air-ground integrated networks: Channel estimation, reliable transmission, and multiple access," *IEEE Wirel. Commun.*, vol. 31, no. 2, pp. 105–111, Apr. 2024.

[12] C. Liu, X. Liu, D. W. K. Ng, and J. Yuan, "Deep residual learning for channel estimation in intelligent reflecting surface-assisted multi-user communications," *IEEE Trans. Wirel. Commun.*, vol. 21, no. 2, pp. 898–912, Feb. 2022.

[13] J. Ye, S. Dang, B. Shihada, and M.-S. Alouini, "Space-air-ground integrated networks: Outage performance analysis," *IEEE Trans. Wirel. Commun.*, vol. 19, no. 12, pp. 7897–7912, Dec. 2020.

[14] K. Guo, M. Lin, B. Zhang, J.-B. Wang, Y. Wu, W.-P. Zhu, and J. Cheng, "Performance analysis of hybrid satellite-terrestrial cooperative networks with relay selection," *IEEE Trans. Veh. Technol.*, vol. 69, no. 8, pp. 9053–9067, Aug. 2020.

[15] H. Shuai, K. Guo, K. An, and S. Zhu, "NOMA-based integrated satellite terrestrial networks with relay selection and imperfect SIC," *IEEE Access*, vol. 9, pp. 111 346–111 357, Aug. 2021.

[16] X. Cai, J. Rodríguez-Piñeiro, X. Yin, N. Wang, B. Ai, G. F. Pedersen, and A. P. Yuste, "An empirical air-to-ground channel model based on passive measurements in LTE," *IEEE Trans. Veh. Technol.*, vol. 68, no. 2, pp. 1140–1154, Feb. 2019.

[17] H. Xing, G. Chen, and G. Wu, "Relay selection algorithm for air–ground cooperative communication based on system capacity and joint user equalization," *IEEE Access*, vol. 13, pp. 179 861–179 874, Oct. 2025.

[18] Z. Su, J. Zhang, K. Wang, X. Duan, Y. Cai, L. Ning, L. Liu, and B. Ai, "A novel GBSM for LEO satellite-ground communication large-scale channels," *IEEE Internet Things J.*, vol. 12, no. 8, pp. 11 049–11 063, Apr. 2025.

[19] W. Khawaja, I. Guvenc, and R. H. Jacobsen, "Propagation channel modeling for LEO satellite missions using ray-tracing simulations," in *Proc. IEEE Wirel. Commun. Net. Conf. (WCNC), Kuala Lumpur, Malaysia*, Apr. 2026, pp. 1–6.

[20] Z. Lou, J. Xu, B. E. Y. Belmekki, and M.-S. Alouini, "SAGSIN: Modeling and analysis of maritime terminals under diverse QoS requirements," *IEEE Trans. Wirel. Commun.*, vol. 25, pp. 17 180–17 194, May 2026.

[21] Y. Gu, R. Wang, D. Wu, Y. Cui, P. He, and B. Yang, "Multi-dimensional modeling and connectivity analysis for THz space-air-ground integrated network," *IEEE Trans. Wirel. Commun.*, vol. 24, no. 6, pp. 4549–4563, Jun. 2025.

[22] X. Hu, B. Lin, X. Lu, P. Wang, N. Cheng, Z. Yin, and W. Zhuang, "Performance analysis of end-to-end LEO satellite-aided shore-to-ship communications: A stochastic geometry approach," *IEEE Trans. Wirel. Commun.*, vol. 23, no. 9, pp. 11 753–11 769, Sep. 2024.

[23] E. M. Mohamed, M. Ahmed Alnakhli, and M. M. Fouda, "Joint UAV trajectory planning and LEO-sat selection in SAGIN," *IEEE Open J. Commun. Soc.*, vol. 5, pp. 1624–1638, Mar. 2024.

[24] K.-X. Li, X. Gao, and X.-G. Xia, "Channel estimation for LEO satellite massive MIMO OFDM communications," *IEEE Trans. Wirel. Commun.*, vol. 22, no. 11, pp. 7537–7550, Nov. 2023.

[25] Z. Lian, L. Jiang, C. He, and D. He, "User grouping and beamforming for HAP massive MIMO systems based on statistical-eigenmode," *IEEE Wirel. Commun. Letters*, vol. 8, no. 3, pp. 961–964, Jun. 2019.

[26] C. Guo, X. Chen, J. Yu, and Z. Xu, "Design of joint device and data detection for massive grant-free random access in LEO satellite internet of things," *IEEE Internet Things J.*, vol. 10, no. 8, pp. 7090–7099, Apr. 2023.

[27] F. Riera-Palou, G. Femenias, M. Caus, M. Shaat, and A. I. Pérez-Neira, "Scalable cell-free massive MIMO networks with LEO satellite support," *IEEE Access*, vol. 10, pp. 37 557–37 571, Apr. 2022.

[28] T. Van Chien, E. Lagunas, T. M. Hoang, S. Chatzinotas, B. Ottersten, and L. Hanzo, "Space-terrestrial cooperation over spatially correlated channels relying on imperfect channel estimates: Uplink performance analysis and optimization," *IEEE Trans. Commun.*, vol. 71, no. 2, pp. 773–791, Feb. 2023.

[29] J. Zhang, Y. Zhang, X. Zhang, W. Wang, and Y. Cao, "SDN-enabled multi-edge access and cache strategy in satellite terrestrial integrated networks," *IEEE Trans. Consum. Electron.*, vol. 71, no. 1, pp. 402–418, Feb. 2025.

[30] K. Yang, T. Røste, F. Bekkadal, and T. Ekman, "Channel characterization including path loss and doppler effects with sea reflections for mobile radio propagation over sea at 2 GHz," in *2010 Int. Conf. Wireless Commun. and Signal Process. (WCSP), Suzhou, China*, 2010, pp. 1–6.

[31] Y. Zeng, R. Zhang, and T. J. Lim, "Throughput maximization for UAV-enabled mobile relaying systems," *IEEE Trans. Commun.*, vol. 64, no. 12, pp. 4983–4996, Dec. 2016.

[32] K.-F. Chen, Y.-C. Liu, and Y. T. Su, "On composite channel estimation in wireless massive MIMO systems," in *Proc. IEEE Glob. Commun. (GLOBECOM) Workshops, Atlanta, GA, USA*, Dec. 2013, pp. 135–139.

[33] G. Bacci, A. Alberto D'Amico, and L. Sanguinetti, "MMSE channel estimation in large-scale MIMO: Improved robustness with reduced complexity," *IEEE Trans. Wirel. Commun.*, vol. 23, no. 12, pp. 18 563–18 575, Dec. 2024.

[34] D. S. Michalopoulos, H. A. Suraweera, G. K. Karagiannidis, and R. Schober, "Amplify-and-forward relay selection with outdated channel estimates," *IEEE Trans. Commun.*, vol. 60, no. 5, pp. 1278–1290, May 2012.

[35] A. Al-Jumaily, A. Sali, V. P. G. Jiménez, F. P. Fontán, M. J. Singh, A. Ismail, Q. Al-Maatouk, A. M. Al-Saegh, and D. Al-Jumeily, "Evaluation of 5G coexistence and interference

signals in the C-Band satellite earth station," *IEEE Trans. Veh. Technol.*, vol. 71, no. 6, pp. 6189–6200, Jun. 2022.

[36] H. M. Hussien, K. Katzis, L. P. Mfupe, and E. T. Bekele, "Capacity, coverage and power profile performance evaluation of a novel rural broadband services exploiting TVWS from high altitude platform," *IEEE Open J. Comput. Soc.*, vol. 3, pp. 86–95, Jun. 2022.

[37] J. Peng, P. Hong, and K. Xue, "Performance analysis of switching strategy in LTE-A heterogeneous networks," *J. Commun. Netw.*, vol. 15, no. 3, pp. 292–300, Jun. 2013.

[38] T. L. Nguyen, G. Kaddoum, T. Nhu Do, and Z. J. Haas, "Ground-to-AAV and RIS-assisted AAV-to-ground communication under channel aging: Statistical characterization and outage performance," *IEEE Trans. Commun.*, vol. 73, no. 9, pp. 8062–8079, Sep. 2025.

[39] Z. Lin, J. Yang, Y. Chen, C. Xu, and X. Zhang, "Maritime distributed computation offloading in space-air-ground-sea integrated networks," *IEEE Commun. Lett.*, vol. 28, no. 7, pp. 1614–1618, Jul. 2024.

[40] K. Xiong, X. Chen, and M. Ying, "Robust beamforming design for integrated satellite-terrestrial maritime communications in the presence of wave fluctuation," *IEEE Internet Things J.*, vol. 11, no. 21, pp. 35 568–35 579, Nov. 2024.